



# Preparation of vertically aligned $\text{WO}_3$ nanoplate array films based on peroxotungstate reduction reaction and their excellent photoelectrocatalytic performance



Qingyi Zeng <sup>a</sup>, Jinhua Li <sup>a</sup>, Jing Bai <sup>a</sup>, Xuejin Li <sup>a</sup>, Ligang Xia <sup>a</sup>, Baoxue Zhou <sup>a,b,\*</sup>

<sup>a</sup> School of Environmental Science and Engineering, Shanghai Jiao Tong University, Shanghai 200240, China

<sup>b</sup> Key Laboratory of Thin Film and Microfabrication Technology, Ministry of Education, Shanghai 200240, China

## ARTICLE INFO

### Article history:

Received 21 June 2016

Received in revised form 8 September 2016

Accepted 23 September 2016

Available online 23 September 2016

### Keywords:

Photoelectrocatalytic

$\text{WO}_3$

Nanoplate

Capping effect

Water splitting

## ABSTRACT

Here, we developed a novel, facile, controllable and scalable method based on peroxotungstate reduction reaction to prepare vertically aligned  $\text{WO}_3$  nanoplate array (NPA) films with preferentially exposed highly reactive (002) facets used in efficient photoelectrocatalytic (PEC) applications. In this method, a slow and controllable reduction of peroxotungstates by ethanol was used, which was the critical step to ensure the uniform and ordered synthesis of orthorhombic  $\text{WO}_3 \cdot \text{H}_2\text{O}$  NPA films which assembled directly on F-doped tin oxide substrates under the capping effect of oxalate, and subsequently  $\text{WO}_3 \cdot \text{H}_2\text{O}$  NPA films were converted into monoclinic  $\text{WO}_3$  NPA films by calcination. The effects of synthetic temperature and time, and the concentration of oxalate on the crystalline phase and morphology of the  $\text{WO}_3 \cdot \text{H}_2\text{O}$  films were studied systematically. The  $\text{WO}_3$  NPA film annealed at an optimized temperature of 500 °C exhibited the highest water splitting current density of ~1.42 mA/cm<sup>2</sup> at 1.23 V vs RHE in 0.1 M  $\text{Na}_2\text{SO}_4$  under AM 1.5 G illumination. It was further improved by decorating with a Co–Pi co-catalyst, which achieved a more stable current density of ~1.95 mA/cm<sup>2</sup> with an incident photon-to-current conversion efficiency of ~51% at 400 nm. The  $\text{WO}_3$  NPA film also showed excellent stability and efficiency (rate constant ~0.8127 h<sup>-1</sup>) for PEC degradation of methylene blue.

© 2016 Elsevier B.V. All rights reserved.

## 1. Introduction

Photoelectrocatalytic (PEC) techniques have received a lot of attention because they provide insight into the utilization of solar energy for producing hydrogen [1–17], degrading organic pollutants [18,19], and generating electricity [20–22]. A pivotal challenge to realize PEC applications in practice is developing suitable photoelectrode materials. To date, many types of semiconductor metal oxides, such as  $\text{TiO}_2$  [1,2],  $\text{WO}_3$  [11–13,23–40], and  $\alpha\text{-Fe}_2\text{O}_3$  [14–17], have been intensely investigated as photoelectrodes because of their highly chemical stability in oxidation conditions and reasonably high incident light-to-current conversion efficiencies. Among them,  $\text{WO}_3$  is a promising photoanode material for its relatively narrow band gap of 2.5–2.7 eV that can absorb approximately 12% of solar light with a theoretical maximum conversion efficiency of ~6.3% [11–13]. Additionally,  $\text{WO}_3$

possesses a moderate hole diffusion length (~150 nm) that is longer than those of  $\alpha\text{-Fe}_2\text{O}_3$  (2–4 nm) and  $\text{TiO}_2$  (~100 nm), thus showing inherently good electron transport properties [12]. The valence band edge of  $\text{WO}_3$  is located at approximately 3.0 V vs NHE [13], which provides a sufficient potential for both the oxidation of water and degradation of organic waste. Although the conduction band edge of  $\text{WO}_3$  is not negative enough for spontaneous hydrogen evolution, it is possible to overcome this drawback by applying an external bias or by coupling the  $\text{WO}_3$  photoanode with a suitable photocathode to achieve water splitting [22].

The PEC performance of  $\text{WO}_3$  films has been substantially improved by synthesizing orderly nanostructured morphologies [23–34], combining with other photocatalysts [35,36], doping [37,38], or decorating with co-catalysts [39,40]. For example, various  $\text{WO}_3$  films with perpendicularly oriented nanostructures have been fabricated, such as nanowire arrays and nanoplate/nanoflake arrays via hydrothermal methods [23–29], nanorod arrays via chemical vapor deposition (CVD) and DC magnetron sputtering (DCMS) [30,31], and nanotube arrays via flame vapor deposition (FVD) and anodization [32,33]. These vertically aligned nanostructured arrays show a significant advantage over nanoparticle films

\* Corresponding author at: School of Environmental Science and Engineering, Shanghai Jiao Tong University, Shanghai 200240, China.

E-mail address: [zhoubaoxue@sjtu.edu.cn](mailto:zhoubaoxue@sjtu.edu.cn) (B. Zhou).

because they can provide direct pathways for much faster electron transport. However, nanoparticle films have numerous grain boundaries, inhibiting the transfer of charges to the back-contacted conductive substrate [29,41]. In addition, ordered nanostructured films with preferential exposure of their active facets can further improve the PEC properties of photoelectrodes [23]. Although the reported methods can prepare well-ordered  $\text{WO}_3$  nanostructures, they are not suitable for the large-scale and economical preparation of nanostructured films for practical applications due to their inherent drawbacks. For example, the hydrothermal method needs an autoclave for generating supercritically high pressures, the CVD, DCMS and FVD methods are complicated and vacuum dependent, and anodization requires costly W foils. Therefore, there is an urgent and practical need to design an economical, simple and efficient method for the large-scale preparation of perpendicularly oriented nanostructured  $\text{WO}_3$  films [42].

Here, we developed a facile, controllable and scalable method based on the unique chemical characteristics of tungstate to prepare vertically aligned  $\text{WO}_3$  nanoplate array (NPA) films used in efficient PEC water splitting and an organic pollutant treatment. This method involves four steps:

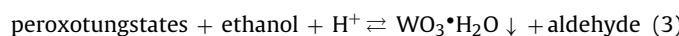
i) The precipitation of tungstic acid: the sodium tungstate solution was fully precipitated in a strong acid medium with excess HCl, which ensured the precipitate was uniform tungstic acid ( $\text{H}_2\text{WO}_4$ , see Fig. S1) [43].



ii) The formation of peroxotungstates: the tungstic acid was dissolved by  $\text{H}_2\text{O}_2$  to form soluble peroxotungstates [44,45].



iii) The reduction of peroxotungstates and the growth of uniform and ordered  $\text{WO}_3 \cdot \text{H}_2\text{O}$  films: the peroxotungstates were slowly and controllably reduced via a weak reductant, ethanol, accompanied by the synthesis of uniform and ordered  $\text{WO}_3 \cdot \text{H}_2\text{O}$  films under facile water-bath conditions.



This is the critical step of the novel method because the slow and controllable reduction of peroxotungstates ensures the uniformly and orderly growth of  $\text{WO}_3 \cdot \text{H}_2\text{O}$  NPA films by adjusting the synthetic temperature, time, and etc.

iv) The annealing of  $\text{WO}_3 \cdot \text{H}_2\text{O}$  films to obtain  $\text{WO}_3$  films.



The single-crystal rectangular  $\text{WO}_3 \cdot \text{H}_2\text{O}$  nanoplates directly grew on the F-doped tin oxide (FTO) substrate, and were assembled layer-by-layer with preferential growth orientations of [100] and [001] along the crystal face of (020) due to the capping effect of oxalate. Monoclinic  $\text{WO}_3$  NPA films with preferentially exposed highly reactive (002) facets were obtained by annealing  $\text{WO}_3 \cdot \text{H}_2\text{O}$  NPA films. The effect of the annealing temperature on the PEC water splitting performance of the as prepared films was studied in detail. A PEC organic pollutant degradation treatment using the  $\text{WO}_3$  NPA film was also studied. All of the results demonstrated that vertically aligned  $\text{WO}_3$  NPA films can be prepared via an economical, facile and scalable strategy for potentially cost-effective and efficient PEC water splitting and wastewater treatment.

## 2. Experimental

### 2.1. Preparation of $\text{WO}_3$ NPA films

The purchased FTO coated glass substrate ( $7.3 \Omega/\text{cm}$ ) was cut into  $3 \times 3 \text{ cm}$  slides and washed under ultrasonication with acetone and deionized water for 30 min. In a typical preparation process (see Fig. 1), 0.4 g of  $\text{Na}_2\text{WO}_4 \cdot 2\text{H}_2\text{O}$  and 0.15 g of capping agent (ammonium oxalate,  $((\text{NH}_4)_2\text{C}_2\text{O}_4)$ ) were dissolved in 33 mL of deionized water (pH 8.6), and 9 mL of HCl (37%) was added to this solution with strong agitation to fully precipitate the  $\text{H}_2\text{WO}_4$  (suspension, pH  $\sim 0.82$ , Eq. (1)). Then, 8 mL of  $\text{H}_2\text{O}_2$  (37%) was added into this suspension with strong agitation for 10 min (pH  $\sim 0.75$ ). The precipitates were dissolved to form a clear solution (Eq. (2)). Next, 30 mL of ethanol was added as a reductant with more strong agitation for 10 min to obtain a clear and stable solution (pH  $\sim 0.53$ ). The FTO glass was dipped into this solution with the FTO side facing down. The synthesis was carried out at  $85^\circ\text{C}$  in a constant temperature bath (heating rate of  $5^\circ\text{C}/\text{min}$ ) and then allowed to cool naturally. The as-prepared film was rinsed with deionized water for 1 min and dried at  $50^\circ\text{C}$  for 10 h. The effect of the annealing temperature was investigated at  $200^\circ\text{C}$ ,  $250^\circ\text{C}$ ,  $300^\circ\text{C}$ ,  $400^\circ\text{C}$ ,  $500^\circ\text{C}$  and  $600^\circ\text{C}$  for 2 h with a heating and cooling rate of  $1^\circ\text{C}/\text{min}$ .

### 2.2. Characterization

The morphologies and microstructures of the samples were investigated by FE-SEM (Sirion200, Philips, Netherlands) and TEM (JEM-2100F, JEOL, Japan). The crystal phase of the samples was characterized with X-ray diffractometry (XRD) (AXS-8 Advance, Bruker, Germany). Raman spectra were recorded on SENTERRA R200 system (Bruker, Germany) with a laser excitation of 532 nm. The X-ray photoelectron spectroscopy (XPS) spectra were measured with an AXIS Ultra DLD (Kratos, Shimadzu) using non-chromatic Al  $K\alpha$  radiation at 12 kV and 25 mA. The UV-visible absorption spectra of the samples were obtained with a UV-Vis photospectrometer (TU-1901, Pgeneral, China). The incident-photon-to-charge conversion efficiency (IPCE) was measured by a system operated with a monochromator (Zolix, China), a 500 W xenon arc lamp, a calibrated silicon photodetector, and a power meter. The detailed PEC tests were given in the Supplementary information.

## 3. Results and discussion

### 3.1. Characterization of the as prepared films

The  $\text{WO}_3$  films were prepared via a new developed method based on the facile and controllable reduction of peroxotungstates as shown in Fig. 1. The mainly possible reactions during the synthesis were described as Eqs. (1)–(4). The Supplementary information provides detailed preparation processes and discusses the effects of the synthetic time and temperature, and the concentration of the capping agent on the morphologies and nanostructures of the as prepared films (Fig. S2–S10). For each parameter, the optimal value was 200 min,  $85^\circ\text{C}$  and 0.15 g, respectively, for synthesizing vertically aligned nanostructures. The results also indicate that the reduction of peroxotungstates was slow and controllable, which was essential to uniformly and orderly growth of the nanostructured films. As shown in Figs. 1 and Fig. S5, the as prepared film was bright yellow and uniform, tightly adhering to the FTO substrate. After annealing at  $500^\circ\text{C}$  for 2 h, the color changed into light olive. The X-ray diffractometry (XRD) patterns shown in Fig. 2a indicate that the as prepared film consisted of orthorhombic tungsten oxide monohydrate ( $\text{WO}_3 \cdot \text{H}_2\text{O}$ ) according to JCPDS no. 43-0679. Com-

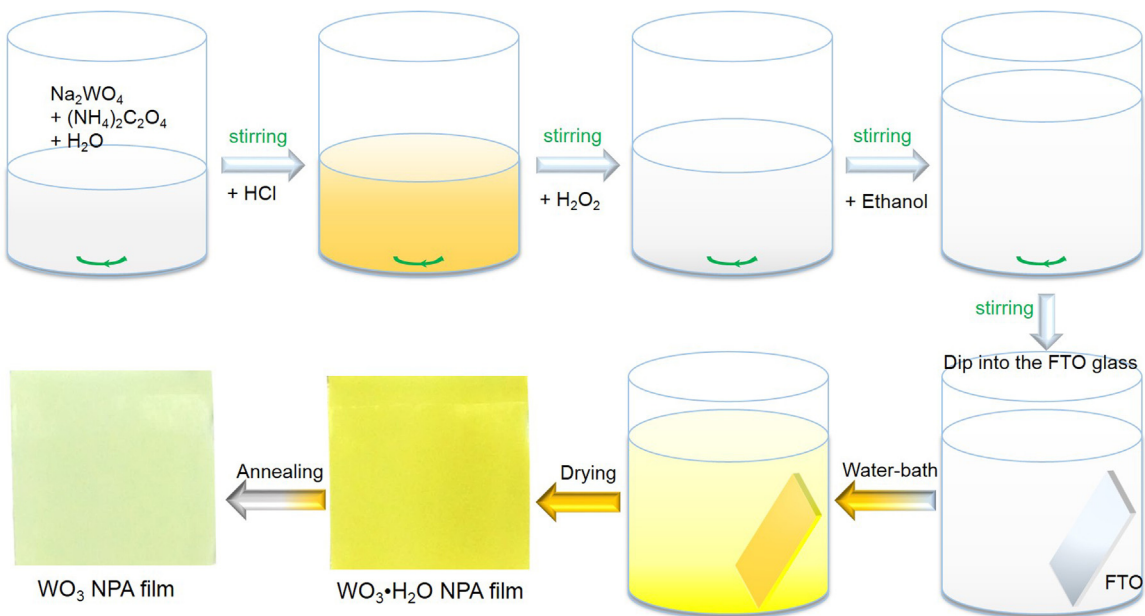


Fig. 1. A flow diagram of the procedure used to synthesize the  $\text{WO}_3$  NPA film.

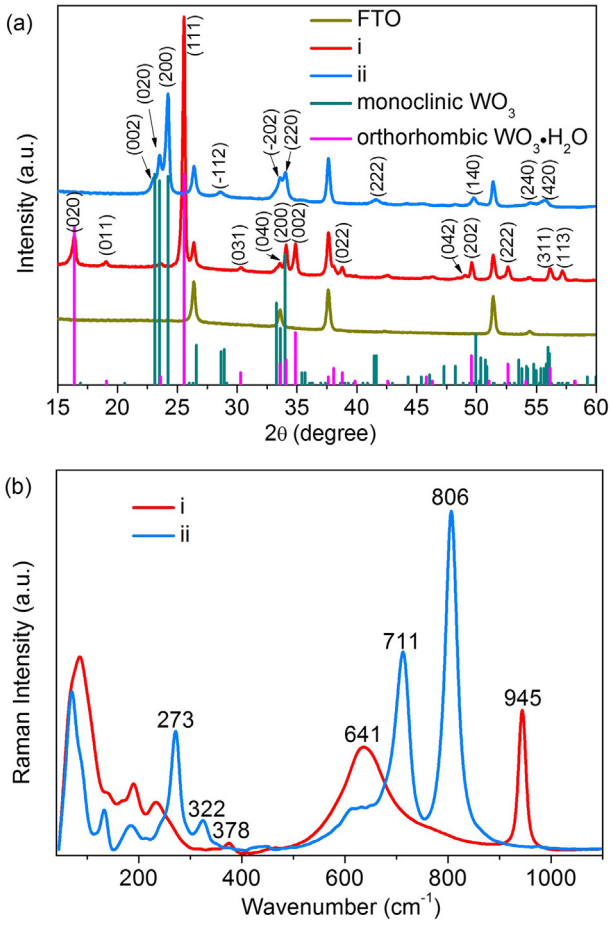


Fig. 2. (a) XRD patterns and (b) Raman patterns of (i) the as prepared film and (ii) the film annealed at  $500^\circ\text{C}$  for 2 h.

pared with the powder diffraction pattern, the (020) diffraction peak was relatively low, which indicates that the [020] direction of the  $\text{WO}_3\text{-H}_2\text{O}$  crystal was parallel to the substrate. The XRD patterns of the annealed film reveal that orthorhombic  $\text{WO}_3\text{-H}_2\text{O}$

film completely converted into monoclinic  $\text{WO}_3$  film after heat-treatment (JCPDS no. 43-1035). A peak that is attributable to the monoclinic  $\text{WO}_3$  (002) facet was of relatively low intensity, suggesting [002] direction was parallel to the substrate. Moreover, the intensified (200) diffraction peak revealed that [200] direction was vertical to the substrate.

Fig. 2b presents the Raman spectra of the as prepared film and the annealed film. The Raman spectra of the as prepared film exhibit two strong peaks: a broad peak centred at  $641\text{ cm}^{-1}$  and a sharp peak located at  $945\text{ cm}^{-1}$ , both of which are the characteristic stretching vibrations of orthorhombic  $\text{WO}_3\text{-H}_2\text{O}$  [46,47], corresponding to the stretching vibrations of the  $\text{W}^{6+}\text{-O}$  bond and the terminal short  $\text{W}^{6+}\text{-O}$  bond, respectively. The weak peak at  $378\text{ cm}^{-1}$  is linked to the stretching of the  $\text{W-OH}_2$  bond [49]. After annealing at  $500^\circ\text{C}$  for 2 h, the Raman spectra are in accordance with monoclinic type  $\text{WO}_3$ : two  $\text{W}^{6+}\text{-O}$  stretching vibrations at  $711\text{ cm}^{-1}$  and  $806\text{ cm}^{-1}$ , and two  $\text{W}^{6+}\text{-O}$  bending vibrations at  $273\text{ cm}^{-1}$  and  $322\text{ cm}^{-1}$  [46–48]. The lattice vibrations below  $200\text{ cm}^{-1}$  are observed in both Raman spectra [49]. The Raman results confirm the XRD result that the as prepared film was orthorhombic  $\text{WO}_3\text{-H}_2\text{O}$  and converted into monoclinic  $\text{WO}_3$  after annealing via the dehydration of hydroxyl groups in the crystalline  $\text{WO}_3\text{-H}_2\text{O}$  (Fig. S11) [29].

Fig. 3 shows the SEM and TEM images of the  $\text{WO}_3\text{-H}_2\text{O}$  film and the  $\text{WO}_3$  film. The top-view SEM images in Fig. 3a and b show that both the  $\text{WO}_3\text{-H}_2\text{O}$  film and the  $\text{WO}_3$  film had plate-like morphologies perpendicular to the substrate (i.e., NPA film). After annealing treatment, the average thickness of the plates was slightly reduced from  $\sim 130\text{ nm}$  to  $\sim 100\text{ nm}$ . This result is in agreement with the reported changes during annealing hydrothermal orthorhombic  $\text{WO}_3\text{-H}_2\text{O}$  nanoplates to monoclinic  $\text{WO}_3$  nanoplates [28,29,50]. From the cross-sectional SEM images in Fig. 3a and b, the thickness of the film remained almost the same at  $\sim 850\text{ nm}$  after calcination. Furthermore, the NPA films tightly adhered to the FTO substrate, and the film was directly grown on the substrate without a seed layer, which is always necessary for hydrothermal strategies [24,26,27,29]. This direct growth strategy may eliminate the grain boundaries from the seed layer, which would result in lower resistance between the photocatalyst and the conductive substrate and thus higher photoelectrocatalytic (PEC) performance. Fig. 3c

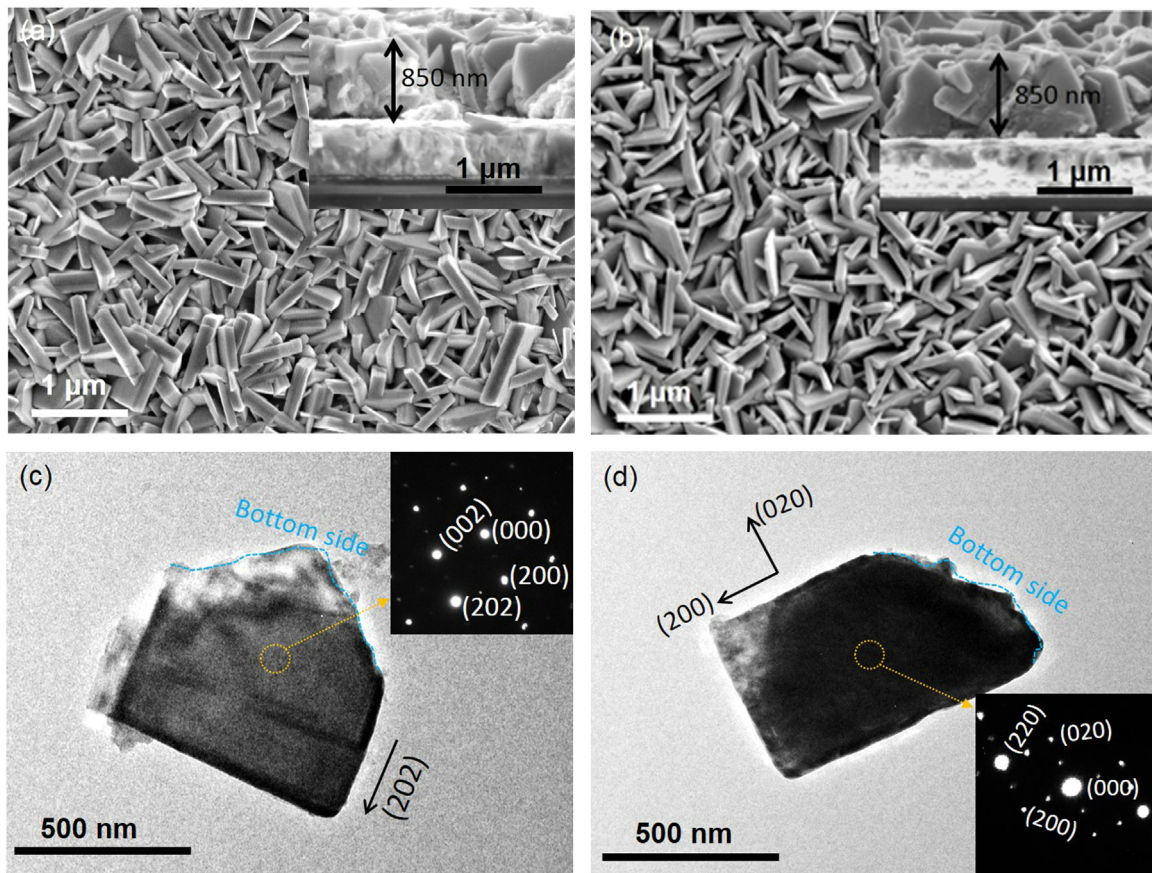


**Fig. 3.** (a) and (b) are the top-view SEM images of the  $\text{WO}_3 \cdot \text{H}_2\text{O}$  and  $\text{WO}_3$  NPA films, respectively, and the inserts are the corresponding cross-sectional SEM images; (c) and (d) are the TEM images of the  $\text{WO}_3 \cdot \text{H}_2\text{O}$  and  $\text{WO}_3$  NPA films, respectively, and the inserts are the SAED patterns.

and d present the TEM images with their corresponding selected area electron diffraction (SAED) patterns of single  $\text{WO}_3 \cdot \text{H}_2\text{O}$  and  $\text{WO}_3$  plates, respectively. The clear SAED patterns indicate that  $\text{WO}_3 \cdot \text{H}_2\text{O}$  plates and  $\text{WO}_3$  plates were very crystalline. Taken from the XRD results shown in Fig. 2a, the corresponding lattice planes are indicated in the SAED patterns. The results show that the  $\text{WO}_3 \cdot \text{H}_2\text{O}$  plates grew in the crystal direction of [202] along the crystal face of (020). After annealing, the resulting  $\text{WO}_3$  plates had a preferential exposure of (002) facets along the crystal directions of [200] and [020]. These results are in accordance with the XRD results shown in Fig. 2a. Because the dehydration of hydroxyl groups in crystalline  $\text{WO}_3 \cdot \text{H}_2\text{O}$  occurs along the [010] direction [28,29,50], the thickness of the  $\text{WO}_3 \cdot \text{H}_2\text{O}$  plates decreased because the crystal transformation induced a shrinkage in the interlayer distance after annealing, while the change was small in the planar size (Fig. S11).

### 3.2. The effect of annealing temperature

Raman, XRD, SEM, TEM and X-ray photoelectron spectroscopy (XPS) were conducted to study the physical and physicochemical properties of the samples annealed at various temperatures. The Raman (Fig. 4) and XRD (Fig. S12) results indicate that monoclinic  $\text{WO}_3$  appeared when annealed at  $250^\circ\text{C}$ , and the crystallinity of the  $\text{WO}_3$  NPA film increased gradually with the elevation of the annealing temperature, which is also demonstrated by the TEM and SAED results (Fig. S13). As indicated by the purple frame in Fig. 4, the characteristic stretching vibration of orthorhombic  $\text{WO}_3 \cdot \text{H}_2\text{O}$  at  $\sim 945 \text{ cm}^{-1}$  is still exhibited in the samples annealed at  $250^\circ\text{C}$  and  $300^\circ\text{C}$ , which indicates that the terminal short  $\text{W}^{6+}-\text{O}$  bond of

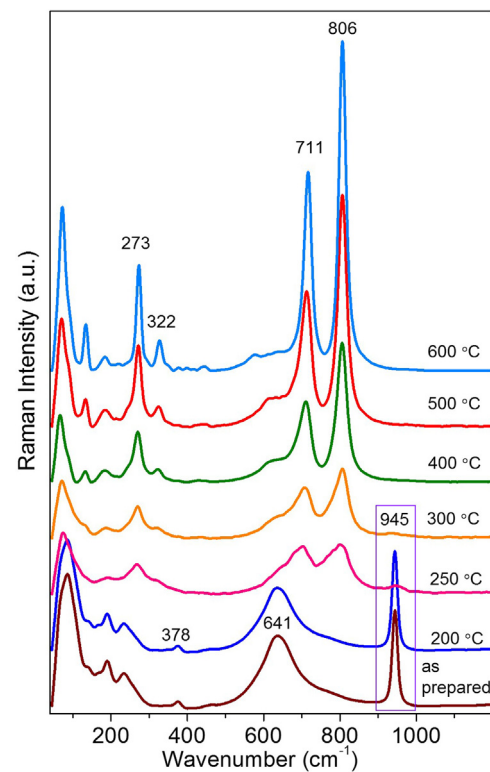


**Fig. 4.** Raman spectra of the films annealed at various temperatures.

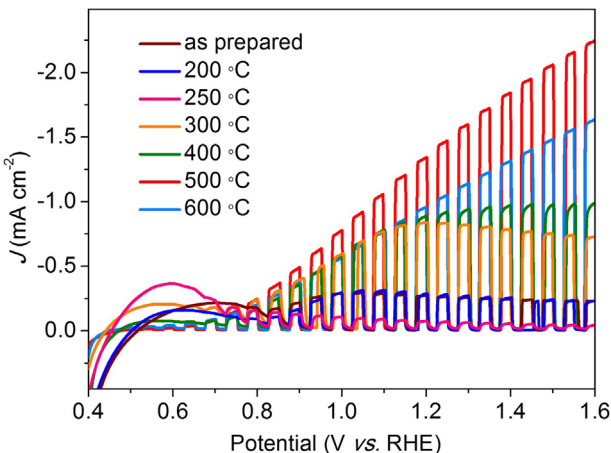


**Fig. 5.** Chopped photocurrent-potential (*J*-*V*) plots of the films annealed at various temperatures.

orthorhombic  $\text{WO}_3 \cdot \text{H}_2\text{O}$  is residual in these samples [46]. The SEM images of the samples annealed with different temperatures further indicated that the average thicknesses of the nanoplates were decreased with the increased annealing temperature (Fig. S14). The sample annealed at 600 °C possessed the highest crystallinity among the as prepared samples (Fig. 4) while it suffered sintering as shown in Fig. S15, which is reflected by the XRD patterns (Fig. S12) because the (200) diffraction peak decreased compared to the sample annealed at 500 °C. The sintering of nanoplates introduced some cavitas in the  $\text{WO}_3$  blocks (Fig. S13e). The XPS result (Fig. S16) indicates that samples annealed at 250 °C and 300 °C had inferior crystallinity and W–O–O–W groups could be formed in these samples, because the peak positions of both O 1s and W 4f showed positive-shifts compared to the well crystalline samples. The effect of the annealing temperature on the light absorption properties of the samples were also studied (Fig. S18).

Fig. 5 shows the chopped photocurrent-potential (*J*-*V*) curves of the films annealed at different temperatures tested in 0.1 M  $\text{Na}_2\text{SO}_4$  under AM 1.5 irradiation (100 mW/cm<sup>2</sup>) from 0.4 to 1.6 V vs RHE with a scan rate of 5 mV/s. It can be seen that the sample annealed at 500 °C showed the highest photocurrent response among the tested samples with a photocurrent density of ~1.42 mA/cm<sup>2</sup> at 1.23 V vs RHE and a maximum photocurrent density of ~2.25 mA/cm<sup>2</sup> at 1.6 V vs RHE (the photocurrent density would further raise as the potential increased, see Fig. S19), which is higher than most previously reported nanostructured  $\text{WO}_3$  films [24–29]. Compared with a typical spin-coated  $\text{WO}_3$  nanoparticle film which showed a photocurrent density of ~0.44 mA/cm<sup>2</sup> at 1.23 V vs RHE under AM 1.5 irradiation [51], the  $\text{WO}_3$  NPA film after annealed at 500 °C showed an improvement of 323%. However, all the samples annealed below 500 °C exhibited a decrease in photocurrent at relatively higher voltages, and the sample annealed at 250 °C suffered the most severe decay.

In a PEC water splitting system, photogenerated electrons in the photoanode can transfer to the counter electrode (Pt) to reduce  $\text{H}^+$  to hydrogen, and the photogenerated holes can cause a series of oxidation reaction, such as  $\text{OH}^- + \text{h}^+ \rightarrow \cdot\text{OH}$ ,  $2\text{H}_2\text{O} + 2\text{h}^+ \rightarrow \text{H}_2\text{O}_2 + 2\text{H}^+$ , etc. For  $\text{WO}_3$  films, the appearance of peroxide species and hydroxy radicals near the surface cause a layer of peroxy species to form at the  $\text{WO}_3$  surface, which can impede the charge transfer at the  $\text{WO}_3||\text{electrolyte}$  interface [52]. For the  $\text{WO}_3 \cdot \text{H}_2\text{O}$  films, the situation is similar. During the *J*-*V* test, the separation efficiency of electron/hole pairs in the films improved with the increase in potential (i.e., an increase in current density), accompanied by the accumulation of peroxy species at the film surface. The resistance caused by the peroxy species layer can, depending on the thickness

of the layer, compete with the effect of the potential; thus, the current density can decay. As the *J*-*V* plots indicate, the formation of peroxy species was easier on the  $\text{WO}_3 \cdot \text{H}_2\text{O}$  film and the samples with inferior crystallinity, which caused an earlier or more severe deactivation on the *J*-*V* curve (Fig. 5). With the superior crystallinity of the samples annealed at 500 °C and 600 °C, the formation of peroxy species was more difficult, which is why there was no decay in the current density during the *J*-*V* test on those samples. Furthermore, the lower crystallinity of the samples annealed at 200 °C, 300 °C and 400 °C can weaken the charge transport properties of the film and increase the recombination of electron/hole pairs because of the large amount of defects, therefore causing the lower PEC performances, although the surface areas of these samples are similar as the sample annealed at 500 °C. For the sample annealed at 600 °C, the relatively lower current density can be partially attributed to the sintering of the plate-like morphology (Fig. S15), which reduced the surface area, and partially to the increased resistance of the FTO substrate (Fig. S20). In general, 500 °C is the optimal temperature for preparing  $\text{WO}_3$  NPA films for PEC applications.

### 3.3. The effect of Co-Pi co-catalyst

$\text{WO}_3$  NPA films were decorated with a cobalt–phosphate (Co–Pi) co-catalyst (Co–Pi/ $\text{WO}_3$  NPA) to improve the water oxidation kinetics on the photoanodes [53–55]. The EDX measurement of 300 s Co–Pi/ $\text{WO}_3$  NPA indicates that Co–Pi was uniformly decorated on the  $\text{WO}_3$  NPA film (Fig. S21), although the XRD result (Fig. S22) shows no obvious diffraction peak of Co–Pi due to the small portion of Co–Pi. The TEM result further demonstrates that the Co–Pi layer of the 300 s Co–Pi/ $\text{WO}_3$  NPA uniformly coated on the  $\text{WO}_3$  nanoplates, and the average thickness of the Co–Pi layer was about 11 nm (Fig. S23). After decorating with Co–Pi, the onset potential for water splitting decreased under both light illumination and in the dark (Fig. 6a), which indicates that Co–Pi facilitated the water oxide reaction occurring at the  $\text{WO}_3||\text{electrolyte}$  interface. Compared with the pristine  $\text{WO}_3$  NPA film, the 300 s Co–Pi/ $\text{WO}_3$  NPA film showed a remarkably increased photocurrent response of ~1.95 mA/cm<sup>2</sup> at 1.23 V vs RHE and a maximum photocurrent density of ~2.95 mA/cm<sup>2</sup> at 1.6 V vs RHE. The Nyquist plots of these samples (Fig. 6b) indicate that Co–Pi decreased the resistance of the  $\text{WO}_3$  NPA films for PEC water splitting, and the 300 s Co–Pi/ $\text{WO}_3$  NPA film exhibited the lowest resistance. This result indicates that the charge transfer at the electrode–electrolyte interface was improved in the presence of Co–Pi co-catalyst as Co–Pi facilitates water oxidation kinetics at the film surface. However, a thicker Co–Pi layer, as in the case of 400 s Co–Pi/ $\text{WO}_3$  and 500 s Co–Pi/ $\text{WO}_3$  NPA films, will increase the resistance of the Co–Pi layer itself and finally reduce its charge transfer properties. In this case, 300 s is an optimized deposition time for decorating Co–Pi on the  $\text{WO}_3$  NPA film.

The stability tests of the  $\text{WO}_3$  and 300 s Co–Pi/ $\text{WO}_3$  NPA films are shown in Fig. 6c. The photocurrent density of the  $\text{WO}_3$  NPA film decreased from ~1.45 mA/cm<sup>2</sup> to ~1.26 mA/cm<sup>2</sup> after 3600 s, and for the 300 s Co–Pi/ $\text{WO}_3$  NPA film, the photocurrent density decreased from ~1.97 mA/cm<sup>2</sup> to ~1.85 mA/cm<sup>2</sup>. The  $\text{WO}_3$  NPA and the 300 s Co–Pi/ $\text{WO}_3$  NPA film decayed by ~13.1% and ~6.1%, respectively, both of which are much lower than the photocurrent decreases of the reported nanostuctured  $\text{WO}_3$  films (~28.4% within 40 min) [25]. Furthermore, the decay percentage of the 300 s Co–Pi/ $\text{WO}_3$  NPA film was only half of that of the  $\text{WO}_3$  NPA film, which means that Co–Pi improved the stability of the film. As discussed above, the deactivation of  $\text{WO}_3$  films may be due to the build-up of a peroxy species layer at the  $\text{WO}_3$  surface, which can impede the charge transfer at the interface between the  $\text{WO}_3$  and the electrolyte. However, the Co–Pi on the  $\text{WO}_3$  film prevents the formation of peroxy species because the Co–Pi co-catalyst can capture the

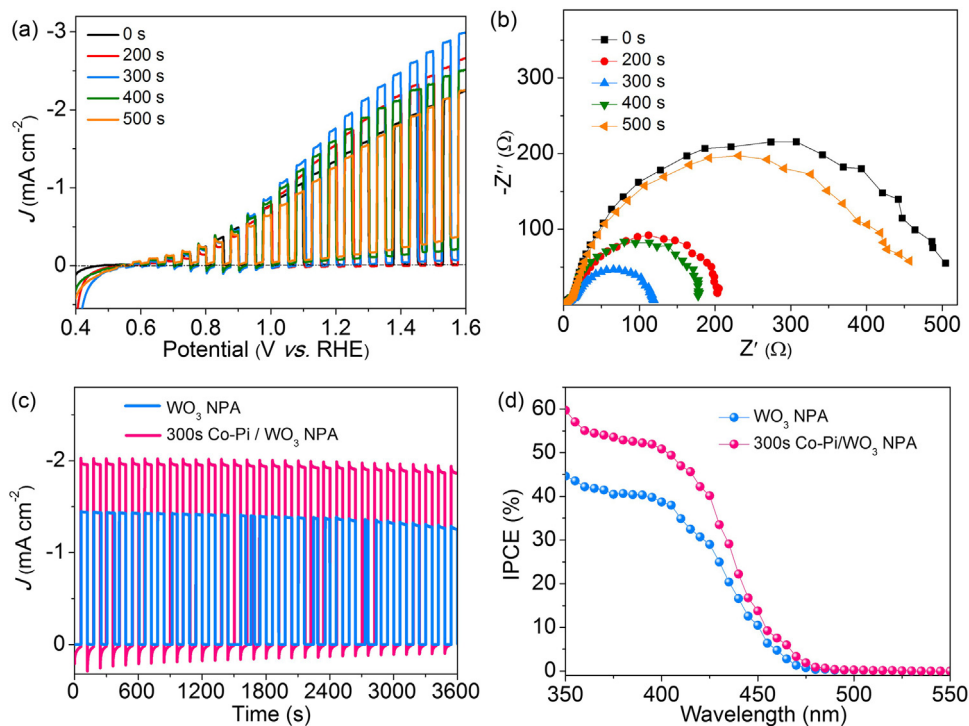


**Fig. 6.** (a) Chopped J-V curves of the Co-Pi/WO<sub>3</sub> NPA films with various photo-assisted electrodeposition times; (b) Nyquist plots of the Co-Pi/WO<sub>3</sub> NPA films under 1.23 V vs RHE; (c) Photocurrent-time and (d) IPCE plots of the WO<sub>3</sub> and 300 s 300s Co-Pi/WO<sub>3</sub> NPA films measured at 1.23 V vs RHE.

majority of photogenerated holes to evolve oxygen rather than generating peroxide species [52]. Therefore, the 300 s Co-Pi/WO<sub>3</sub> NPA film possessed a higher stability than the WO<sub>3</sub> NPA film. As can be seen from the SEM images of these tested samples (see Fig. S24a and b), after decorating with Co-Pi co-catalyst, the Co-Pi/WO<sub>3</sub> NPA film corrosion is smaller than the pristine WO<sub>3</sub> NPA film, which further demonstrates that the stability of the WO<sub>3</sub> NPA film is enhanced via decorating with Co-Pi co-catalyst.

Both the WO<sub>3</sub> and 300 s Co-Pi/WO<sub>3</sub> NPA films exhibited incident-photon-to-charge conversion efficiency (IPCE) behavior in the range of 350 to 470 nm (Fig. 6d), which is roughly consistent with the light absorption spectrum of the WO<sub>3</sub> NPA film. This means that the conversion of the absorbed photons into photocurrent occurred successfully in the photoanodes. An IPCE value of ~51% was obtained for the Co-Pi/WO<sub>3</sub> NPA film at 400 nm, and for the WO<sub>3</sub> NPA film, the value was ~38%. After applying the Co-Pi co-catalyst, the IPCE values improved considerably when compared with the pristine WO<sub>3</sub> NPA film in the entire response region, which indicates that the Co-Pi co-catalyst facilitates the conversion of the absorbed photons into photocurrent.

#### 3.4. Properties of PEC degradation of MB

The PEC properties of degrading organic pollutants of the WO<sub>3</sub> NPA films were investigated by degradation experiments of methylene blue (MB). The PEC (at a bias potential of 1 V), photocatalytic (PC, i.e., without a bias potential), and direct photolytic (DP) degradations of MB in neutral aqueous solutions were performed under the given conditions. The UV-vis absorption spectra of MB solutions for various PEC reaction times are shown Fig. 7a. The characteristic peak of MB (at 665 nm) was found to decrease steadily with the reaction time. As seen in Fig. 7b and c, the degradation rate of MB in different systems follows the tendency of PEC > PC > DP. The highest rate constant of ~0.8127 h<sup>-1</sup> was obtained by the PEC system, which is ~1.93 and ~7.68 times higher than that of PC (~0.4205 h<sup>-1</sup>) and DP (~0.1058 h<sup>-1</sup>), respectively. The results indi-

cate that the degradation efficiency of MB can be improved under the photocatalysis of the WO<sub>3</sub> NPA film, especially by applying a positive bias on the film to facilitate the separation of photogenerated electron-hole pairs. The repeated use tests shown in Fig. 7d indicate that the WO<sub>3</sub> NPA film is also stable for PEC wastewater treatment. The SEM image (Fig. S24c) shows that this WO<sub>3</sub> NPA film appears corrosion after six PEC cycles for MB degradation, which can be also due to the formation of peroxy species as aforementioned. Nonetheless, the degrading efficiencies did not show decrease in the repeated use tests as the organics also can be degraded by the peroxy species.

#### 3.5. Possible formation mechanism of the films

Thanks to the facile and controllable nature of this synthesis method, the formation mechanism of the WO<sub>3</sub>•H<sub>2</sub>O NPA film is easily to be investigated. The effect of synthetic time on the morphology of the WO<sub>3</sub>•H<sub>2</sub>O films are provided in Figs. S7 and S8. To further reveal the detailed morphological change from the lichen-like porous thin film to the plate-like film, the samples prepared with synthetic times of 45 min, 50 min, 55 min and 60 min are provided in Fig. 8. The SEM images show that some laminas were overlaid on the vertically oriented laminas layer by layer, becoming thicker and more plate-like. (NH<sub>4</sub>)<sub>2</sub>C<sub>2</sub>O<sub>4</sub> plays an important role as a capping agent in controlling the morphology during the synthesis of WO<sub>3</sub>•H<sub>2</sub>O NPA films (Fig. S9). C<sub>2</sub>O<sub>4</sub><sup>2-</sup> is an electron-rich organic ion; in this case, C<sub>2</sub>O<sub>4</sub><sup>2-</sup> can form H-bonds with the interlayer H<sub>2</sub>O molecules of orthorhombic WO<sub>3</sub>•H<sub>2</sub>O on the (010) facet (Fig. 9a), which means the growth along [010] can be restricted, thus forming the laminas structure (Fig. 8a). Furthermore, the adsorbed C<sub>2</sub>O<sub>4</sub><sup>2-</sup> on adjacent laminas can connect via H-bonds with free H<sub>2</sub>O, as shown schematically in Fig. 9a, which would result in polymerization between these laminas (Fig. 8b). Consequently, plates replaced the irregular laminas (Fig. 8c), and the plates grew along the (010) facet and became thicker layer by layer, which is evident in the mature WO<sub>3</sub>•H<sub>2</sub>O nanoplates (see Fig. 8e and f). Moreover, the

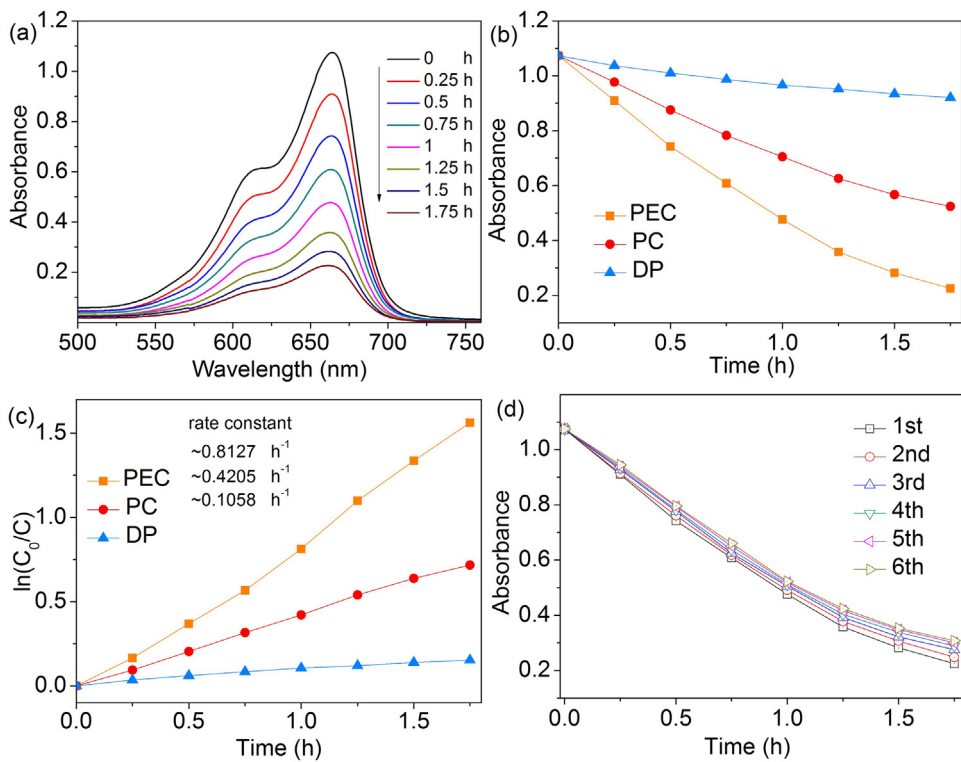


**Fig. 7.** (a) UV–vis absorption spectra of MB solution at 15 min intervals during the PEC degradation reaction on a  $\text{WO}_3$  NPA film at a bias potential of 1 V vs SCE; (b) degradation of MB under PEC, PC and DP conditions and (c) the corresponding kinetic curves; (d) the repeated use of the  $\text{WO}_3$  NPA film for MB degradation over six PEC cycles.

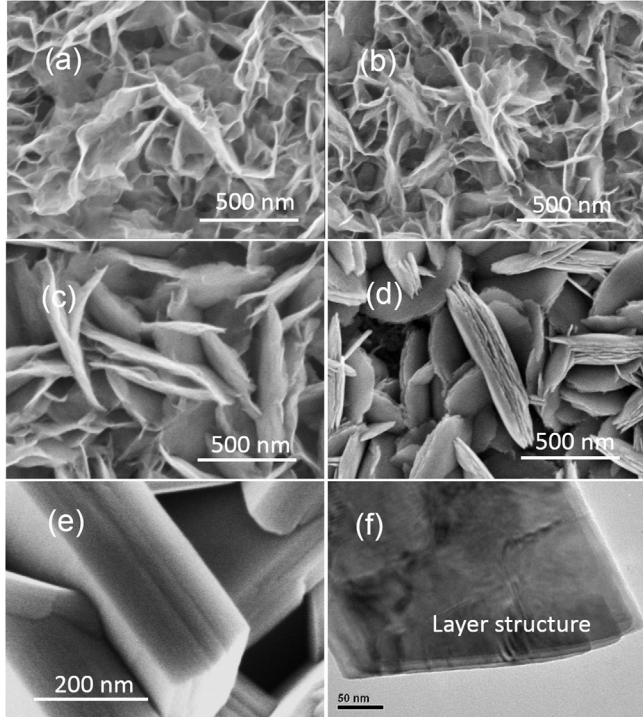


**Fig. 8.** Top-view SEM images of the as prepared films with synthetic times of (a) 45 min, (b) 50 min, (c) 55 min and (d) 60 min; (e) The high resolution SEM image and (f) the TEM image of an as prepared  $\text{WO}_3 \cdot \text{H}_2\text{O}$  nanoplate.

geometrical shape of the nanoplates changed from round to rectangular (see Fig. S7) with a preferential orientation of [202] on the (020) crystal face, which implies that the growth rates of the orthorhombic  $\text{WO}_3 \cdot \text{H}_2\text{O}$  along the [100] and [001] orientations are

faster than other directions in this system. Therefore, the rectangular  $\text{WO}_3 \cdot \text{H}_2\text{O}$  nanoplates were assembled layer-by-layer with preferential growth orientations of [100] and [001] along the crystal face of (020). The as prepared  $\text{WO}_3 \cdot \text{H}_2\text{O}$  NPA films can be transformed into monoclinic  $\text{WO}_3$  NPA films by dehydration during annealing (Figs. 9b and Fig. S11). This transformation led to both the change of lattice orientation and the decrease in the thicknesses of nanoplates, which were confirmed by the XRD, SEM and SAED results (see Figs. 2a and 3).

Preferentially exposing the active facets of nanocrystals is an effective way to improve their photocatalytic/PEC reactivity [56,57]. The resulting  $\text{WO}_3$  NPA film had a preferential exposure of the (002) facet, which possesses the highest surface energy ( $1.56 \text{ J/m}^2$ ) compared with the (020) facet ( $1.54 \text{ J/m}^2$ ) and the (200) facet ( $1.43 \text{ J/m}^2$ ) [23], which suggests that the (002) facet is more favorable in adsorbing reaction species to decrease the surface energy. In addition, the dangling O atoms on the (002) facets, which belong to the weakest W–O bond in the monoclinic  $\text{WO}_3$  (Fig. S11), provide abundant binding sites for  $\text{H}_2\text{O}$  and organics (H–R) via H-bonds (Fig. 9b). Consequently, photo-generated holes are more readily consumed on the (002) facets by the generation of active oxygen species, water oxidation (Fig. S25) and the degradation of organics, which reduces the recombination of electrons and holes. Therefore, the remarkable PEC performances of the  $\text{WO}_3$  NPA films in water splitting and degrading MB can be attributed to the preferential exposure of highly reactive (002) facets. Furthermore, the seed-free growth of the as prepared films is another reason for the improved PEC properties because of the enhanced charge transfer from the  $\text{WO}_3$  to the FTO substrate.

To verify the feasibility of the large-scale preparation of the  $\text{WO}_3$  NPA films using our method, we prepared  $\text{WO}_3 \cdot \text{H}_2\text{O}$  NPA films on various sizes of substrates:  $3 \times 3 \text{ cm}$ ,  $5 \times 5 \text{ cm}$ ,  $10 \times 10 \text{ cm}$  and  $20 \times 20 \text{ cm}$  as shown in Fig. 10. All the deposited films are uniformly colored, which demonstrates the excellent homogeneity of

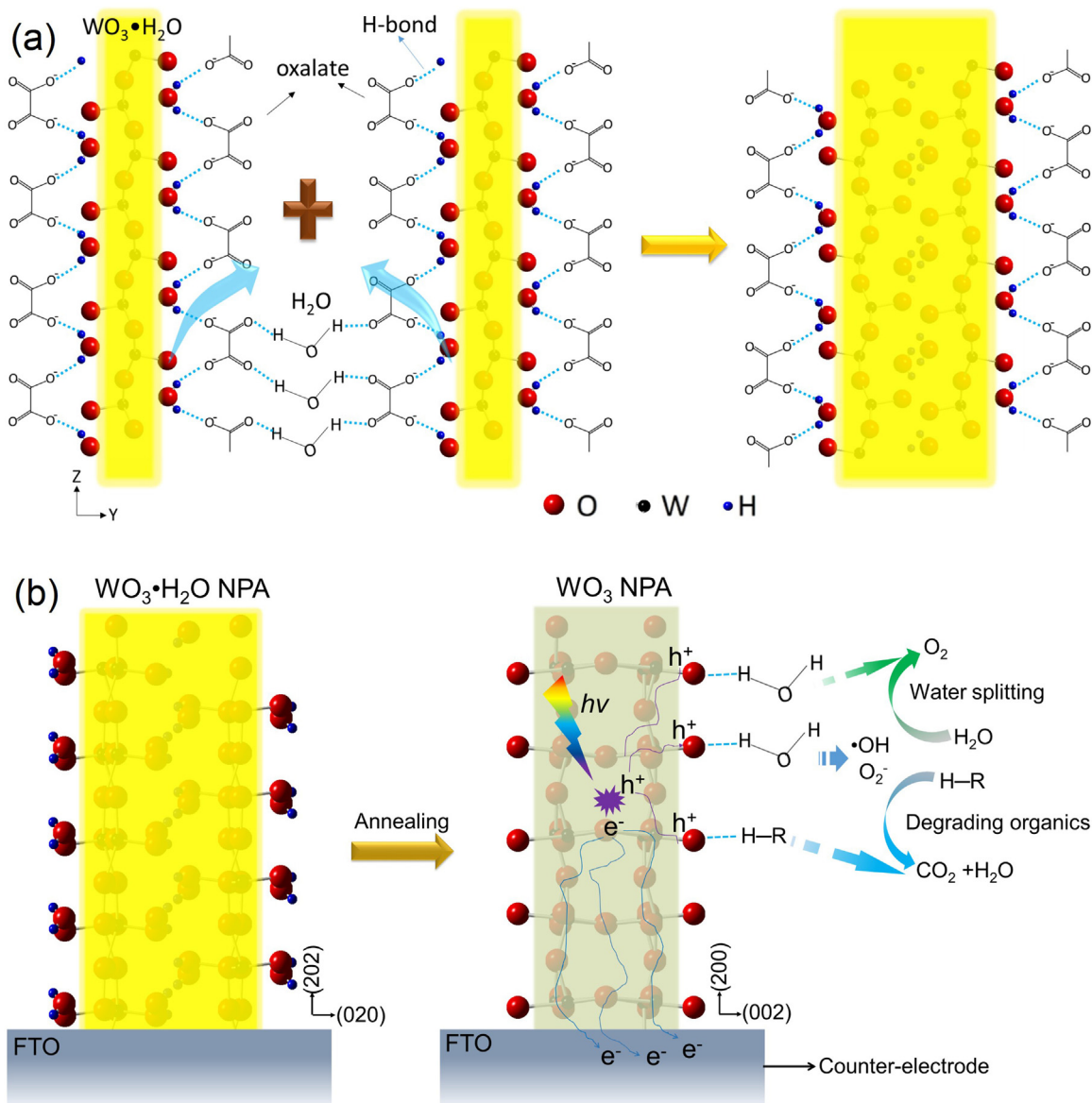


**Fig. 9.** (a) A possible mechanism for the layer-by-layer formation of  $\text{WO}_3 \cdot \text{H}_2\text{O}$  nanoplates; (b) the transformation of the orthorhombic  $\text{WO}_3 \cdot \text{H}_2\text{O}$  NPA film into the monoclinic  $\text{WO}_3$  NPA film, and possible mechanisms for the PEC water splitting and organic degradation on the (002) facet of the  $\text{WO}_3$  NPA film.

the  $\text{WO}_3 \cdot \text{H}_2\text{O}$  NPA films. This result indicates that our method is able to prepare  $\text{WO}_3$  NPA films on large-scale substrates, which can be attributed to the facile nature of this method and it is meaningful in practical applications.

#### 4. Conclusion

In summary, we have demonstrated a novel method based on peroxotungstate reduction reaction to prepare vertically aligned  $\text{WO}_3$  NPA films for efficient PEC applications. Perpendicularly oriented  $\text{WO}_3 \cdot \text{H}_2\text{O}$  NPA films assembled layer-by-layer with preferential growth orientations of [100] and [001] along the (020) crystal face directly on FTO substrates via a controlled reduction of peroxotungstates by ethanol in water-bath condition, and then converted to  $\text{WO}_3$  NPA films by annealing. Without using any costly chemicals, or any high temperature and high pressure, or any sophisticated control system, this method is facile, economical and suitable for large-scale preparation of  $\text{WO}_3$  NPA films. The film morphology was mainly controlled by the synthetic time, tem-

perature, and the amount of  $(\text{NH}_4)_2\text{C}_2\text{O}_4$ . For each parameter, the optimal value was 200 min, 85 °C and 0.15 g, respectively. The  $\text{WO}_3$  NPA film annealed at 500 °C for 2 h exhibited a PEC water splitting current of  $\sim 1.42 \text{ mA/cm}^2$  at 1.23 V vs RHE. After coating with a Co-Pt co-catalyst, a more higher and stable current density of  $1.95 \text{ mA/cm}^2$  with an IPCE of  $\sim 51\%$  at 400 nm was achieved. The  $\text{WO}_3$  NPA film also demonstrated excellent stability and degradation efficiency in treating simulated organic wastewater in the PEC degradation tests. The excellent PEC performances of the  $\text{WO}_3$  NPA film can be attributed to both the seed-free growth of the film and the preferential exposure of the highly reactive (002) facets. This study provides a useful reference for the design and fabrication of stable and large-scale nanostructured  $\text{WO}_3$  films for potentially cost-effective and efficient PEC applications.

#### Acknowledgements

The authors would like to acknowledge the National Nature Science Foundation of China (No. 51578332, No. 21576162,



**Fig. 10.** The photograph of the as prepared  $\text{WO}_3 \cdot \text{H}_2\text{O}$  NPA films on various sizes of substrates: 3 × 3 cm, 5 × 5 cm, 10 × 10 cm and 20 × 20 cm.

No. 21276153, No. 21507085) and Shanghai Yangfan Program (14YF1401500) for financial support.

## Appendix A. Supplementary data

Supplementary data associated with this article can be found, in the online version, at <http://dx.doi.org/10.1016/j.apcatb.2016.09.045>.

## References

- [1] A. Fujishima, K. Honda, *Nature* 238 (1972) 37–38.
- [2] X. Chen, S. Shen, L. Guo, S.S. Mao, *Chem. Rev.* 110 (2010) 6503.
- [3] S.Y. Noh, K. Sun, C. Choi, M. Niu, M. Yang, K. Xu, S. Jin, D. Wang, *Nano Energy* 2 (2013) 351–360.
- [4] M. Liu, D. Jing, Z. Zhou, L. Guo, *Nat. Commun.* 4 (2013) 2278.
- [5] Y. Yang, H. Zhang, Z.H. Lin, Y. Liu, J. Chen, Z. Lin, Y.S. Zhou, C.P. Wong, Z.L. Wang, *Energy Environ. Sci.* 6 (2013) 2429–2434.
- [6] X. Chen, Z. Zhang, L. Chi, A.K. Nair, W. Shangguan, Z. Jiang, *Nano-Micro Lett.* 8 (2016) 1–12.
- [7] W.K. Chang, S.J. Yeob, H.M. Cheng, Y.S. Kang, *Energy Environ. Sci.* 8 (2015) 3646–3653.
- [8] Z. Haider, Y.S. Kang, *ACS Appl. Mater. Interfaces* 6 (2014) 10342–10352.
- [9] S.W. Shin, J.Y. Lee, K.S. Ahn, S.H. Kang, H.K. Jin, *J. Phys. Chem. C* 119 (2015) 13375–13383.
- [10] H.S. Kim, D.T. Nguyen, E.-C. Shin, J.-S. Lee, S.K. Lee, K.-S. Ahn, S.H. Kang, *Electrochim. Acta* 114 (2013) 159–164.
- [11] R. Solarska, R. Jurczakowska, J. Augustynski, *Nanoscale* 4 (2012) 1553–1556.
- [12] S.S. Kalanur, Y.J. Hwang, S.Y. Chae, O.S. Joo, *J. Mater. Chem. A* 1 (2013) 3479–3488.
- [13] J. Yang, X. Zhang, H. Liu, C. Wang, S. Liu, P. Sun, L. Wang, Y. Liu, *Catal. Today* 201 (2013) 195–202.
- [14] M.J. Kang, Y.S. Kang, *J. Mater. Chem. A* 3 (2015) 15723–15728.
- [15] G. Wang, Y. Ling, D.A. Wheeler, K.E.N. George, K. Horsley, C. Heske, J.Z. Zhang, *Y. Li, Nano Lett.* 11 (2011) 3503–3509.
- [16] D.A. Wheeler, G. Wang, Y. Ling, Y. Li, J.Z. Zhang, *Energy Environ. Sci.* 5 (2012) 6682–6702.
- [17] Q. Zeng, J. Bai, J. Li, L. Xia, K. Huang, X. Li, B. Zhou, *J. Mater. Chem. A* 3 (2015) 4345–4353.
- [18] L. Zhu, M. Hong, G.W. Ho, *Nano Energy* 11 (2015) 28–37.
- [19] J. Bai, B. Zhou, *Chem. Rev.* 114 (2014) 10131–10176.
- [20] Y. Yan, J. Fang, Z. Yang, J. Qiao, Z. Wang, Q. Yua, K. Sun, *Chem. Commun.* 49 (2013) 8632–8634.
- [21] Q. Zeng, J. Bai, J. Li, Y. Li, X. Li, B. Zhou, *Nano Energy* 9 (2014) 152–160.
- [22] Q. Chen, J. Li, X. Li, K. Huang, B. Zhou, W. Shangguan, *ChemSusChem* 6 (2013) 1276–1281.
- [23] J. Zhang, P. Zhang, T. Wang, J. Gong, *Nano Energy* 11 (2015) 189–195.
- [24] J.Y. Zheng, G. Song, C.W. Kim, Y.S. Kang, *Nanoscale* 5 (2013) 5279–5282.
- [25] J. Yang, W. Li, J. Li, D. Sun, Q. Chen, *J. Mater. Chem.* 22 (2012) 17744–17752.
- [26] Y.O. Kim, K.-S. Ahn, S.H. Kang, *Mater. Lett.* 151 (2015) 28–30.
- [27] W. Li, P. Da, Y. Zhang, Y. Wang, X. Lin, X. Gong, G. Zheng, *ACS Nano* 8 (2014) 11770–11777.
- [28] J.Y. Zheng, G. Song, J. Hong, T.K. Van, A.U. Pawar, D.Y. Kim, C.W. Kim, Z. Haider, Y.S. Kang, *Cryst. Growth Des.* 14 (2014) 6057–6066.
- [29] F. Amano, D. Li, B. Ohtani, *Chem. Commun.* 46 (2010) 2769–2771.
- [30] J. Zhang, W. Zhang, Z. Yang, Z. Yu, X. Zhang, T.C. Chang, A. Javey, *Sensor Actuat. B: Chem.* 202 (2014) 708–713.
- [31] M. Horprathum, T. Srichaiyaperk, B. Samransuksamer, A. Wisitsoraat, P. Eiamchai, S. Limwichean, C. Chananonnawathorn, K. Aiempakanit, N. Nuntawong, V. Pattranasettakul, C. Oros, S. Porntheeraphat, P. Songsiririthigul, H. Nakajima, A. Tuantranont, P. Chindaoudom, *ACS Appl. Mater. Interfaces* 6 (2014) 22051–22060.
- [32] P.M. Rao, I.S. Cho, X. Zheng, P. Combust. Inst. 34 (2013) 2187–2195.
- [33] M. Altomare, O. Pfoch, A. Tighineanu, R. Kirchgeorg, K. Lee, E. Sell, P. Schmuki, *J. Am. Chem. Soc.* 137 (2015) 5646–5649.
- [34] Y.O. Kim, S.-H. Yu, K.-S. Ahn, S.K. Lee, S.H. Kang, *J. Electrochem. Soc.* 162 (2015) H449–H452.
- [35] L.V.C. Lima, M. Rodriguez, V.A.A. Freitas, T.E. Souza, A.E.H. Machado, A.O.T. Patrocílio, J.D. Fabris, L.C.A. Oliveira, M.C. Pereira, *Appl. Catal. B: Environ.* 165 (2015) 579–588.
- [36] Y.R. Smith, B. Sarma, S.K. Mohanty, M. Misra, *Electrochim. Commun.* 19 (2012) 131–134.
- [37] Y. Chang, K. Yu, C. Zhang, R. Li, P. Zhao, L.-L. Lou, S. Liu, *Appl. Catal. B: Environ.* 176–177 (2015) 363–373.
- [38] H. Song, Y. Li, Z. Lou, M. Xiao, L. Hu, Z. Ye, L. Zhu, *Appl. Catal. B: Environ.* 166–167 (2015) 112–120.
- [39] C. Fábrega, S. Murcia-López, D. Monllor-Satoca, J.D. Prades, M.D. Hernández-Alonso, G. Penelas, J.R. Morante, T. Andreu, *Appl. Catal. B: Environ.* 189 (2016) 133–140.
- [40] S.S. Thind, K. Rozic, F. Amano, A. Chen, *Appl. Catal. B: Environ.* 176–177 (2015) 464–471.
- [41] M. Law, L.E. Greene, J.C. Johnson, R. Saykally, P. Yang, *Nat. Mater.* 4 (2005) 455–459.
- [42] R. Sathre, C.D. Scown, W.R. Morrow, J.C. Stevens, I.D. Sharp, J.W. Ager, K. Walczak, F.A. Houleae, J.B. Greenblatt, *Energy Environ. Sci.* 7 (2014) 3264–3278.
- [43] R.L. Graham, L.G. Hepler, *J. Am. Chem. Soc.* 80 (1958) 3538–3540.
- [44] H. Nakajima, T. Kudo, N. Mizuno, *Chem. Mater.* 11 (1999) 691–697.
- [45] K. Kamata, T. Hirano, S. Kuzuya, N. Mizuno, *J. Am. Chem. Soc.* 131 (2009) 6997–7004.
- [46] M. Ahmadi, S. Sahoo, R. Younesi, A.P.S. Gaur, R.S. Katiyar, M. Guinel, *J. Mater. Sci.* 49 (2014) 5899–5909.
- [47] G.N. Kustova, Yu.A. Chesarov, L.M. Plyasova, I.Yu. Molin, A.I. Nizovskii, *Vib. Spectrosc.* 55 (2011) 235–240.
- [48] R.S. Lillard, G.S. Kanner, D.P. Bulf, *J. Electrochem. Soc.* 145 (1998) 2718–2725.
- [49] A. Takase, K. Miyakawa, *Jpn. J. Appl. Phys.* 30 (1991) 1508–1511.
- [50] C. Deliang, G. Lian, Y. Atsuo, K. Kazuyuki, S. small Yoshiyuki, (2008) 1813–1822.
- [51] J. Su, L. Guo, N. Bao, C.A. Grimes, *Nano Lett.* 11 (2011) 1928–1933.
- [52] W. Kim, T. Tachikawa, D. Monllor-Satoca, H. Kim, T. Majima, W. Choi, *Energy Environ. Sci.* 6 (2013) 3732–3739.
- [53] L. Ge, C. Han, X. Xiao, L. Guo, *Appl. Catal. B: Environ.* 142–143 (2013) 414–422.
- [54] S. Hernández, G. Gerardi, K. Bejtka, A. Fina, N. Russo, *Appl. Catal. B: Environ.* 190 (2016) 66–74.
- [55] T. Jin, P. Diao, Q. Wu, D. Xu, D. Hu, Y. Xie, M. Zhang, *Appl. Catal. B: Environ.* 148–149 (2014) 304–310.
- [56] H.G. Yang, C.H. Sun, S.Z. Qiao, J. Zou, G. Liu, S.C. Smith, H.M. Cheng, G.Q. Lu, *Nature* 453 (2008) 638–641.
- [57] G. Xia, J. Ye, *Chem. Commun.* 46 (2010) 1893–1895.